M-SHarC: Multi-Spectral Harmonic Characterization and Classification

Blessing Okoro*, Vaasu Taneja*, Clark Mattoon, Xin Li, Mariya Zheleva
Department of Computer Science, University at Albany, SUNY, USA
{aaokoro, vtaneja, cmattoon, xli48, mzheleva}@albany.edu
*These authors contributed equally.

***Abstract*—Transmitters operating at a fundamental frequency inherently emit harmonics at integer multiples of that frequency, which can interfere with incumbent systems in higher bands, even when the fundamental transmission complies with regulations. This poses a serious interference challenge, especially for sensitive applications such as remote Earth sensing and radio astronomy. However, current methods for detecting and attributing harmonic interference are manual and labor intensive.**

We introduce M-SHarC, a novel approach for characterizing and reconciling faint harmonics with their fundamental frequency. M-SHarC operates on a 3D time-frequency-spectra tensor that captures a transmitter's fundamental and harmonic activity across multiple spectra. It enhances low-SNR inputs using a diffusion model, applies sparse dictionary learning to characterize transmitter and harmonic activity, and reconciles harmonics with their respective fundamentals. We validate M-SHarC in simulation and real-world experiments, demonstrating its ability to detect harmonics at only 3dB above the noise floor, even in the presence of strong incumbent signals. It also blindly classifies whether an observed signal is fundamental or harmonic and determines the harmonic order. To our knowledge, this is the first work to unify fundamental and harmonic analysis into a multispectral framework, enabling scalable, data-driven approaches to interference detection and spectrum enforcement.

I. Introduction

The radio spectrum is used by widely diverse stakeholders including consumer broadband, remote Earth sensing and radio astronomy [1]. The past 20 years have brought a rapid growth of capabilities across all stakeholders both in terms of their instantaneous bandwidths, as well as their tunable range. This leads to the convergence of disparate stakeholders to the same bands, which thus far has been tackled through spectrum-sharing approaches. However, most existing efforts focus only on co-existence at a transmitter's primary operational frequency (also known as its fundamental frequency or first harmonic), while no attention is given to coexistence issues emerging due to out-of-band secondary emissions.

Secondary emissions occur in bands that are outside a technology's designated operational frequency, and can be caused both by transmitters and receivers. They include sideband leakage (caused by transmitters), spurs (caused by receivers) and **harmonics** (caused by transmitters), all of which are becoming increasingly prevalent with the proliferation and densification of wide-band transceivers. There have been documented instances of harmonics impacting incumbent signals for different applications like aeronautical navigation [2] and cellular services [3]. Such secondary emissions have several adverse effects. First, they lead to increased noise floor, which (i) increases the complexity of radio systems to combat out-of-band pollution [4], and (ii) completely prevents high-sensitivity passive/scientific instruments from serving their applications [5], [6], [7]. Additionally, the statistical properties of the noise change, which challenges inherent assumptions in traditional wireless communication models. A second key issue is the direct interference with incumbent systems. These effects, especially when combined, can critically impede our progress in deploying and utilizing spectrum-sharing systems. It is usually up to the entity that suffers out-of-band interference to detect, characterize, reconcile, and advocate against these effects. The process is labor- and equipment-intensive, requires highly-trained personnel, and in some instances has taken years to complete [3]. This calls for novel spectrum measurement and characterization methodologies to aid in out-of-band emission detection and reconciliation.

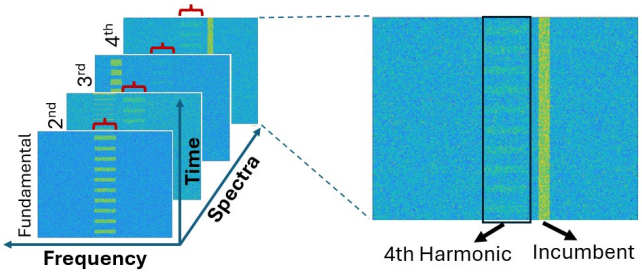

Figure 1: Overview: The goal of multi-spectral transmitter analytics is to detect time-frequency activity across multiple spectrum scans and reconcile harmonic activity with the corresponding fundamental frequency.

Our focus is on out-of-band interference caused by harmonics. The effects of harmonic emissions are illustrated in Fig. 1. The figure presents four stacked illustrative spectrum scans at a transmitter's fundamental frequency, and across three more bands for the 2nd, 3rd and 4th harmonics. While in the fundamental band, the transmitter activity is observed alone, harmonics might be observed alongside or overlapping with incumbents. Thus, ***the goal*** *of harmonic emission detection and characterization is to detect the time-frequency activity at each of the four spectrum scans and reconcile the harmonic activity with its fundamental frequency*. We dub this process ***multi-spectral transmitter analytics***, as it entails the joint characterization and reconciliation of multiple spectra. This goal opens several challenges. First, *how to characterize the time-frequency footprint of ultra-low signal-to-noise ratio*

(SNR) signals, such as those produced by harmonics? Second, *how to perform the above task in the presence of high-SNR incumbents?* Lastly, *how to reconcile the characterized harmonics with their fundamental frequency?*

Existing efforts focus on detecting receiver spurs [8], or out-of-band interference [9], [10], [11], however, no research explores characterizing harmonics and reconciling them with their originator. A plethora of existing work tackles spectrum analytics, including transmitter detection and characterization [12], [13], [14], [15], classification [16], [17], [18], modulation recognition [19], [20], localization [21], [22], anomaly detection [23], [24] and device fingerprinting [25]. However, all of these efforts focus on a transmitter's fundamental band and do not consider multi-spectral harmonic activity.

To address this gap, we develop M-SHarC (Multi-Spectral Harmonic Characterization). It takes as an input a multi-spectral scan of Power Spectral Density (PSD) stored as a 3-D tensor, such as the one illustrated in Fig. 1; and operates in three stages. First, it denoises the input using a custom unsupervised diffusion model inspired by [26]. Second, it characterizes the time-frequency activity in each tensor face, producing bounding boxes around each occupied time-frequency block. To this end, we build on recent work in multi-dictionary sparse representation of spectrum data [14] to robustly detect fundamental and harmonic activity in the presence of co-occurring incumbents. Lastly, M-SHarC employs a pairwise similarity metric inspired by the Jaccard Index to reconcile harmonics with their fundamental activity.

We evaluate M-SHarC in simulation, with over-the-air (OTA) traces from a USRP-based [27] lab testbed, and from an in-situ measurement campaign at the National Radio Quiet Zone (NRQZ). We compare against state-of-the-art in fundamental frequency characterization and demonstrate that M-SHarC reliably detects harmonics as close as 2 dB above the noise floor. In low SNR settings, we demonstrate an average accuracy of over 97% with OTA traces and in the presence of incumbents. We further show that M-SHarC can be used to blindly differentiate fundamental from harmonic activity and determine the order of observed harmonics in arbitrary spectrum traces. Finally, we demonstrate harmonic characterization from a public safety station at the NRQZ.

This paper makes the following contributions:

- We conceptualize multi-spectral transmitter analytics to aid the resolution of harmonic interference.
- We design M-SHarC, a framework for high-sensitivity harmonic detection and reconciliation, which uses diffusion-based denoising and multi-dictionary sparse coding.
- We evaluate M-SHarC in simulation and a small testbed and show high performance with extremely low-SNR harmonics and in the presence of incumbents. We demonstrate that M-SHarC can blindly classify the order of observed harmonic.
- M-SHarC is unsupervised and, thus, applicable to any transmitter type.
- We carry out a real-world measurement campaign at the NRQZ and demonstrate M-SHarC's harmonics detection.

II. Related Work

Spectrum data analytics. Prior work on spectrum data analytics has targeted various insights including (i) transmitter detection and detailed characterization of time-frequency occupancy [12], [13], [14], [15], technology classification [16], [17], [18], modulation recognition [19], [20], localization [21], [22], anomaly/interference detection [23], [24] and device fingerprinting [25]. A majority of these methods are supervised, which requires pre-training of (usually deep learning based) models [16], [17], [18], [19], [20]. Such methods suffer poor performance in low-SNR regimes, and with distribution shifts between the training and the testing data [28], [29]. Thus, they are not directly applicable to multi-spectral transmitter characterization, which entails extremely low-SNR signals and cross-spectral distribution shifts. Other efforts focus on unsupervised spectrum characterization [12], [13], [14], [15] to detect all time-frequency bands occupied by a transmitter, and attribute observed activity to individual emitters in multi-transmitter scenarios. Some of these methods are successful in lower-SNR regimes [14], [13], and because they are unsupervised, they are not sensitive to distribution shifts. However, as we show later, their sensitivity is not good enough for the detection and reconciliation of faint harmonics. A key limitation of all existing work is that it targets characterization of a transmitter's fundamental frequency. Our work is the first to consider transmitter characterization as a multi-spectral task.

Out-of-band emission detection has mostly focused on the negative impact of harmonics on scientific applications [9], [10], [11] and radio frontend design [30], [31]. The scientific community has mostly focused on detecting and excising interference from scientific observations, regardless of its cause – harmonics or fundamental activity. In radio frontend design, there is some focus on harmonic cancellation as a hardware design principle [30], [31]. Other work characterizes receiver spurs to detect the presence of passive Wi-Fi eavesdroppers [8]. However, none of these caters to multi-spectral transmitter characterization, which is the focus of this paper.

Spectrum data denoising. Traditional RF signal denoising uses wavelets, which "utilize a series of orthogonal bases with different resolutions to represent or approximate a signal through the expansion and translation of the wavelet basis function" [32]. However, selecting an appropriate wavelet basis is critical, as improper selection degrades performance [32], [33], [34]. Researchers rely on prior domain knowledge [13], [35], [36], [37], experimental trials [34], or algorithmic selection [33] to find suitable wavelets.

Recently, autoencoders have been applied to RF denoising and classification [38], [39], [40], [41]. These self-supervised models encode input data into forms optimal for downstream tasks [39]. Unlike wavelets, autoencoders do not require domain knowledge but do require training on paired noisy-clean signals to minimize reconstruction error [38]. This limits applicability when training data is unavailable or not generalizable. Given that harmonics are extremely low SNR signals, too difficult for wavelets and lacking training data

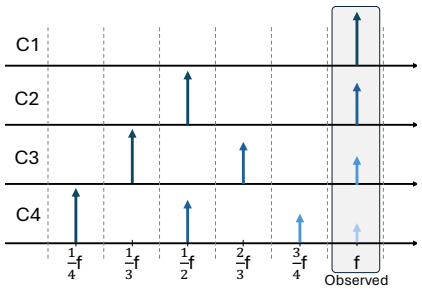

Figure 2: Illustrative example of the goal of multi-spectral characterization. Given an observed band (rightmost pane of the figure), a multi-spectral sensing and analytics framework should be able to discern whether the observed activity is fundamental or harmonic and determine the order of the harmonic.

for autoencoders, we employ a self-supervised diffusion-based denoising methodology that operates directly on input RF traces [26].

Denoising diffusion models. Diffusion models are applied in image synthesis [42], [43], [26] and have recently been considered for denoising in wireless communications [44], [45]. A key limitation of existing diffusion models is their reliance on supervised learning, which often requires large training datasets. This poses a challenge, as collecting and labeling such data is difficult, leading to models that perform well in-distribution but struggle with out-of-distribution data. To address this, [43] introduced conditional diffusion denoising, leveraging a pre-trained model. However, this still requires fine-tuning the pretrained model with additional data. Building on this, [26] proposed a self-supervised diffusion model that incorporates a variational spatio-spectral module (VS2M) for denoising using only the degraded image. Our work extends this approach to RF data denoising, using a similar self-supervised denoising strategy that operates solely on the input RF data, and does not need an additional degraded signal.

III. Multi-spectral characterization

The goal of multi-spectral transmitter characterization in this work is to determine whether observed activity at a *known* frequency corresponds to a fundamental emission or a harmonic, to infer the harmonic order, and to reconcile the observation with its fundamental frequency. Thus, given a spectrum scan in which activity has been identified at some frequency f, our objective is to recover the transmitter's multispectral footprint across fundamental and harmonic bands.

Fig. 2 illustrates this objective through four representative cases, each assuming that transmitter activity is observed at a known frequency f (rightmost pane). The arrows indicate the relative power relationships between the fundamental and harmonic components, with harmonics appearing at significantly lower power due to filter suppression.

- *Case 1:* The activity observed at f corresponds to the fundamental frequency (C1; top pane).
- *Case 2:* The activity observed at f corresponds to the second harmonic (C2; second pane).
- *Case 3:* The activity observed at f corresponds to the third harmonic (C3; third pane).
- *Case 4:* The activity observed at f corresponds to the fourth harmonic (C4; bottom pane).

Harmonics occur at integer multiples of the fundamental frequency. Consequently, once activity is observed at frequency f, the associated harmonics will fall on a unique frequency derivative of f. E.g., if H4 is observed at f (Case 4), then its corresponding H3, H2, and fundamental must occur at $3/4f$, $1/2f$, and $1/4f$, respectively. Similarly, Case 3 implies activity at $2/3f$ and $1/3f$, Case 2 at $1/2f$, and Case 1 implies no additional activity. Across all cases, the union of relevant sensing bands is $\{f, 3/4f, 2/3f, 1/2f, 1/3f, 1/4f\}$. This structure enables a deterministic sensing schedule that supports multispectral reconciliation.

Generalizing from this example, multi-spectral transmitter characterization proceeds in three steps. First, a frequency f at which transmitter activity has been detected or specified a priori is taken as the reference for multispectral exploration. Second, a set of candidate cases $\{\mathrm{C1}, \ldots, \mathrm{C}k\}$ is defined, where k is the highest harmonic order of interest. A loose upper bound on the number of target scan bands is $M = 1 + \sum_{i=1}^{k} i$, although tighter bounds are often possible due to shared bands across cases (for example, both C2 and C4 require measurements at $1/2f$). Finally, the collected multi-band measurements are jointly characterized and reconciled. `M-SHarC` follows this framework, as detailed next.

IV. Methodology

We present a novel framework for harmonic characterization that builds upon diffusion-based denoising and multi-dictionary sparse coding for precise time-frequency activity detection. Our approach consists of three stages: (i) a *denoising* based on an unsupervised diffusion model; (ii) *harmonic characterization* based on sparse dictionary recovery; and (iii) *harmonic reconciliation* with its fundamental frequency.

A. Preliminaries

Due to the extremely low SNR of harmonics, we employ diffusion model-based denoising [42], [43], [26] to enhance detection and characterization. Our input is a 3D Power Spectral Density (PSD) tensor $\mathcal{X} \in \mathbb{R}^{t \times f \times k}$, where t represents time sweeps, f represents frequency bins, and k represents spectral channels corresponding to fundamental and harmonic bands (Fig. 1). Each tensor slice $\mathbf{X} \in \mathbb{R}^{t \times f}$ contains b transmitters $\mathbf{T}_i$ and i.i.d. Gaussian noise ϵ:

$$\mathbf{X} = \sum_{i=1}^{b} \mathbf{T}_i + \epsilon \tag{1}$$

The denoising objective is to transform noisy observations $\mathcal{X}$ into clean representations $\bar{\mathcal{X}}$ suitable for harmonic characterization. Diffusion models learn to reconstruct data by reversing a noise corruption process. Denoising Diffusion Probabilistic Models (DDPM) [42] learn a model distribution $p_\theta(\mathbf{x})$ approximating the data distribution $q(\mathbf{x})$, where $\mathbf{x} \in \mathbb{R}^{t \cdot f \cdot k} = \mathrm{vec}(\mathcal{X})$. The forward process gradually adds Gaussian noise via a Markov chain:

$$q(\mathbf{x}_\tau|\mathbf{x}_0) = \mathcal{N}(\mathbf{x}_\tau; \sqrt{\alpha_\tau}\mathbf{x}_0, (1-\alpha_\tau)\mathbf{I}), \text{ where } \alpha_\tau = \prod_{i=0}^{\tau}(1-\beta_i) \tag{2}$$

where $\beta_\tau \in (0,1)$ is the noise variance at timestep τ, $\mathbf{x}_\tau$ is the data at timestep τ, and $\mathbf{x}_0$ is the observed data.

The reverse process reconstructs clean data from noise by iteratively sampling from a learned posterior: $\mathbf{x}_T \to \mathbf{x}_{T-1} \to \cdots \to \mathbf{x}_1 \to \mathbf{x}_0$. The joint distribution is:

$$p_\theta(\mathbf{x}_{0:T}) := p(\mathbf{x}_T) \prod_{\tau=1}^{T} p_\theta(\mathbf{x}_{\tau-1}|\mathbf{x}_\tau), \tag{3}$$

$$p_\theta(\mathbf{x}_{\tau-1}|\mathbf{x}_\tau) := \mathcal{N}(\mathbf{x}_{\tau-1}; \boldsymbol{\mu}_\theta(\mathbf{x}_\tau, \tau), \boldsymbol{\Sigma}_\theta(\mathbf{x}_\tau, \tau)) \tag{4}$$

where $p(\mathbf{x}_T) = \mathcal{N}(\mathbf{x}_T; 0, \mathbf{I})$ is Gaussian noise, and $\boldsymbol{\mu}_\theta(\mathbf{x}_\tau, \tau)$, $\boldsymbol{\Sigma}_\theta(\mathbf{x}_\tau, \tau)$ are the learned mean and covariance at timestep τ with parameters θ.

Denoising Diffusion Restoration Models (DDRM) [43] extend DDPM to linear inverse problems:

$$\mathbf{y} = \mathbf{H}\mathbf{x} + \mathbf{z}, \tag{5}$$

where $\mathbf{H}$ models degradation (e.g., downsampling for super-resolution, binary masking for inpainting, or identity for denoising) and $\mathbf{z} \sim \mathcal{N}(0, \sigma_\mathbf{y}^2\mathbf{I})$ is additive Gaussian noise.

Spectrum characterization presents unique challenges: acquiring training data requires specialized hardware and expertise; and wireless channel diversity causes distribution shifts that degrade model performance [28]. Self-supervised DDS2M [26] diffusion models address both issues by eliminating training requirements and distribution shift sensitivity. We adopt DDS2M's Variational Spatio-Spectral Module (VS2M), which comprises: (1) untrained spatial and spectral networks and (2) a variational inference-based loss function.

(1) Untrained Spatial and Spectral Networks decompose the input tensor $\mathcal{X} \in \mathbb{R}^{t\times f\times k}$ into spatial (time-frequency) and spectral (cross-band) components using a Linear Mixture Model that learns directly from degraded data:

$$\mathbf{x} = \text{vec}(\mathcal{X}) = \text{vec}\left(\sum_{r=1}^{R} \mathbf{S}_\theta(\mathbf{z_r}) \circ \mathbf{C}_\zeta(\mathbf{w_r})\right), \tag{6}$$

where $\mathbf{S}_\theta(\cdot)$ is an untrained U-Net for spatial patterns, $\mathbf{C}_\zeta(\cdot)$ is an untrained FCN for spectral characteristics, θ, ζ are network parameters, $\mathbf{z}_r, \mathbf{w}_r$ are low-dimensional random vectors, R is the tensor rank representing the number of signal components, and $\circ$ denotes outer product.

(2) Variational Inference-Based Loss ensures the networks learn the posterior distribution via an ELBO objective that aligns the learned posterior with the true distribution:

$$\begin{aligned}&\mathbb{E}_{q(\mathbf{x}_0),q(\mathbf{y}|\mathbf{x}_0)}\left[\log p_{\theta,\zeta}(\mathbf{x}_0|\mathbf{y})\right] \\ &\geq \mathbb{E}_{q(\mathbf{x}_{0:T}),q(\mathbf{y}|\mathbf{x}_0)}\left[\log p_{\theta,\zeta}(\mathbf{x}_{0:T}|\mathbf{y}) - \log q(\mathbf{x}_{1:T}|\mathbf{x}_0, \mathbf{y})\right]\end{aligned} \tag{7}$$

This simplifies to a denoising loss that optimizes the estimated signal $\mathbf{x}_{\theta_\tau,\zeta_\tau}$ at step τ:

$$\arg\min_{\theta,\zeta} \|\mathbf{x}_\tau - \sqrt{\alpha_\tau}\mathbf{x}_{\theta_\tau,\zeta_\tau}\|_F^2 \tag{8}$$

Where:

$$\mathbf{x}_{\theta_\tau,\zeta_\tau} = \text{vec}(\sum_{r=1}^{R} \mathbf{S}_{\theta_\tau}(\mathbf{z_r}) \circ \mathbf{C}_{\zeta_\tau}(\mathbf{w_r})) \tag{9}$$

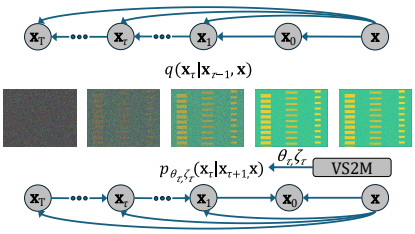

Figure 3: Forward and reverse diffusion processes in M-SHarC, conditioned on input $\mathbf{x}$ without additional degradation. The reverse process uses the VS2M module for self-supervised denoising.

and θ_τ, ζ_τ are the learnable U-Net and FCN parameters, respectively.

B. Multi-spectral RF Denoising

We adapt DDS2M with domain-specific modifications to the linear inverse problem (Eq. 5). RF signals experience inherent degradation from propagation environments that cannot be separated from the observed signal. Thus, we set $\mathbf{H} = \mathbf{I}$ and eliminate the independent additive noise term z, directly conditioning the diffusion model on the noisy observation x without explicit noise modeling.

*1) **Self-Supervised Diffusion Process**:* Our method learns to denoise RF data using only the input itself. The forward diffusion follows Eq. (2), while the reverse is guided by variational inference-based optimization (Eq. (8)).

The VS2M module jointly estimates signal structure through two architectures. The spatial (time-frequency) component uses a U-Net with six encoder-decoder layers: the encoder reduces spatial resolution via max pooling while increasing channels from 16 to 128 (filters: 7×7 to 3×3); the decoder up-samples using nearest neighbor interpolation with skip connections at layers 3-6. LeakyReLU activation, reflection padding, and final sigmoid activation (constraining values to $[0,1]$) are applied throughout. The spectral component uses a four-layer FCN with dimensions $(128, 256, 256, 128)$ to process the band dimension. Both networks are randomly initialized and jointly trained via the variational objective to learn the posterior distribution directly from noisy RF input.

Algorithm 1 M-SHarC's Reverse Diffusion Process

Require: The noisy signal $\mathbf{x}$, the hyperparameters R, τ_0, T, $\beta_{1:\tau_0}$, $\sigma_{1:\tau_0}$, $\sigma_\mathbf{x}$, η, and η_b.
1: Initialize θ_{τ_0}, ζ_{τ_0}, $\mathbf{z}_r$, $\mathbf{w}_r$;
2: Obtain $\mathbf{x}_{\tau_0}$ from Eq. (10)
3: **for** $\tau = \tau_0 - 1$ to 1 **do**
4: Update θ_τ, ζ_t from Eq. (8)
5: Obtain $\mathbf{x}_{\theta_\tau,\zeta_\tau}$ from Eq. (9)
6: Obtain $\mathbf{x}_{\tau-1}$ from Eq.(11)
7: **end for**
Ensure: The denoised image $\mathbf{x}_0$.

*2) **Reverse Diffusion Process**:* Since $\mathbf{H} = \mathbf{I}$, there is no structured degradation to account for in the SVD decomposition, which simplifies the posterior distribution. Algorithm 1

summarizes M-SHarC's reverse diffusion process, which iteratively refines the noisy input $\mathbf{x}$ into a denoised signal $\mathbf{x}_0$ through a series of backward steps from τ_0 to 1.

The algorithm proceeds as follows. Without pre-trained priors, we initialize inference at $\tau_0 = T/2$ rather than T to avoid recovering $\mathbf{x}_0$ from pure Gaussian noise. The posterior at this initialization timestep (step 2) is:

$$p_{\theta_{\tau_0},\zeta_{\tau_0}}(\mathbf{x}_{\tau_0}^{(i)}|\mathbf{x}) = \mathcal{N}\left(\mathbf{x}^{(i)}, \sigma_{\tau_0}^2 - \sigma_{\mathbf{x}}^2\right). \tag{10}$$

This represents a Gaussian distribution centered at the input data $\mathbf{x}$ with variance adjusted based on the noise level. At each reverse step (steps 3-6), we update the network parameters θ_τ, ζ_τ via the variational objective (Eq. (8), step 4), obtain the estimated signal $\mathbf{x}_{\theta_\tau,\zeta_\tau}$ (Eq. (9), step 5), and compute the posterior transition distribution (step 6) as follows:

$$p_{\theta_\tau,\zeta_\tau}(\mathbf{x}_\tau^{(i)}|\mathbf{x}_{\tau+1},\mathbf{x}) = \begin{cases} \mathcal{N}\left(\mathbf{x}_{\theta_\tau,\zeta_\tau}^{(i)} + \sqrt{1-\eta^2}\sigma_\tau \frac{\mathbf{x}^{(i)} - \mathbf{x}_{\theta_\tau,\zeta_\tau}^{(i)}}{\sigma_{\mathbf{x}}}, \eta^2\sigma_\tau^2\right), & \text{if } \sigma_\tau < \sigma_{\mathbf{x}}, \\ \mathcal{N}\left((1-\eta_b)\mathbf{x}_{\theta_\tau,\zeta_\tau}^{(i)} + \eta_b\mathbf{x}^{(i)}, \sigma_\tau^2 - \sigma_{\mathbf{x}}^2\eta_b^2\right), & \text{if } \sigma_\tau \geq \sigma_{\mathbf{x}}. \end{cases} \tag{11}$$

Here $\mathbf{x}_\tau^{(i)}$ and $\mathbf{x}_{\theta_\tau,\zeta_\tau}^{(i)}$ denote the i-th elements of vectors $\mathbf{x}_\tau$ and $\mathbf{x}_{\theta_\tau,\zeta_\tau}$; σ_τ is the noise variance in $\mathbf{x}_\tau$ (dependent on $\beta_{1:T}$); and η, η_b control the injected noise per timestep. This formulation conditions each reverse step on both the previous noisy estimate and the original observation, progressively refining the signal without requiring additional degradation modeling.

C. Harmonic Characterization

After denoising, we characterize time-frequency activity across fundamental and harmonic bands. Our characterization process produces bounding boxes around each contiguous time-frequency block in which a transmitter was detected as active. Traditional energy detection struggles in noisy environments with high false positives or missed detections. Sparse dictionary coding offers a more robust, structured approach by leveraging statistical patterns in RF data.

We build upon SCAN [14], an unsupervised sparse dictionary coding framework, and introduce two key innovations tailored for low-SNR harmonic detection. We apply characterization on a slice-by-slice basis, processing each spectral band (fundamental and harmonics) independently. Algorithm 2 summarizes M-SHarC's characterization process for a single tensor slice, which iteratively detects transmitters through four key steps: (1) row-wise mask-aware centering to enhance signal while suppressing noise; (2) greedy frequency band selection to iteratively isolate transmitters; (3) temporal activity detection to extract transmission patterns; and (4) bookkeeping to determine termination.

The algorithm proceeds as follows for each tensor slice. We begin with a single denoised PSD matrix $\mathbf{X} \in \mathbb{R}^{t\times f}$ (Eq. (1)) corresponding to one spectral band, and initialize a binary detection mask $\mathbf{\Omega} \in \mathbb{R}^{t\times f}$ to all ones and a frequency dictionary $\mathbf{D} \in \mathbb{R}^{f\times p}$ (step 1). The algorithm then iterates through steps 2-7 until all transmitters in the current slice are detected. This process is repeated independently for each tensor slice (fundamental and harmonic bands).

Algorithm 2 M-SHarC Characterization Algorithm

Require: $\mathbf{X} \in \mathbb{R}^{t\times f}$, q, temporal dictionary $\mathbf{\Phi} \in \mathbb{R}^{t\times t}$
Ensure: A set of transmitters $\mathbf{T}$.
1: Initialize mask $\mathbf{\Omega} \leftarrow \mathbf{1}_{t\times f}$, and $\mathbf{D} \in \mathbb{R}^{f\times p}$
2: **while** true **do**
3: Masked row-wise centering of $\mathbf{X}$ to obtain $\mathbf{Z}$ Eq. (12)
4: Greedy frequency band selection Eq. (13)
5: Temporal activity detection Eq. (14)
6: Check stopping criteria, break if satisfied
7: Update $\mathbf{\Omega}$, $\mathbf{T}$ Eq. (15)
8: **end while**

*1) **Input and Row-wise centering**:* At each iteration, we apply mask-aware row-wise centering (step 3) using the binary mask $\mathbf{\Omega}$ that excludes previously detected transmitters:

$$\mathbf{Z} = (\mathbf{X} - \mu_{\mathbf{X}}\mathbf{1}) \odot \mathbf{\Omega} \tag{12}$$

where $\mu_{\mathbf{X}} \in \mathbb{R}^t = [(\mathbf{X}\odot\mathbf{\Omega})\mathbf{1}] \oslash (\mathbf{\Omega}\mathbf{1})$ is the masked row-wise mean, $\odot$ is element-wise multiplication, and $\oslash$ is element-wise division. This enhances the strongest transmitter per row while suppressing noise and weaker signals, enabling detection of one transmitter per iteration.

*2) **Frequency band selection**:* After centering, we identify the transmitter's frequency band (step 4) using the binary dictionary $\mathbf{D}$ with $p = \frac{f(f+1)}{2}$ atoms (columns), where each column represents a contiguous frequency pattern (consecutive 1s). Following an Orthogonal Matching Pursuit (OMP)-like approach, we: (1) compute inner product $\mathbf{ZD}$ to evaluate atom alignment with the centered data; (2) aggregate and normalize scores across time sweeps by atom length $\mathbf{n}$; (3) select the highest-scoring atom:

$$s = \text{max-index}(\mathbf{1ZD} \oslash \mathbf{n}) \quad \mathbf{d}_s = \mathbf{D}(:, s) \tag{13}$$

where $s \in [1, p]$ is the selected atom index and $\mathbf{d}_s$ is the corresponding frequency band.

*3) **Temporal transmitter activity detection**:* After detecting the frequency band, we extract temporal activity within the band (step 5) in three steps: (1) Aggregate PSD values: $\mathbf{a} = \mathbf{X}\mathbf{d}_s$. (2) Obtain sparse representation $\mathbf{w}$ via convex relaxation:

$$\arg\min_{\mathbf{w}} ||\mathbf{a} - \mathbf{\Phi}\mathbf{w}||_2 + \lambda||\mathbf{w}||_1 \tag{14}$$

where $\mathbf{\Phi}$ is the Haar wavelet and λ controls sparsity. The Haar's rectangular shape preserves transmission patterns while ensuring noise robustness. (3) Cluster the smoothed representation $\mathbf{\Phi}\mathbf{w}$ using a two-component GMM to separate signal from noise, and produce a binary activity vector $\mathbf{g}$.

To improve low-SNR detection, we initialize the GMM noise component using statistics from the fundamental band. The fundamental slice, having higher SNR, provides robust noise estimates (mean and standard deviation) that inform

subsequent harmonic slices. This follows the findings in [46], which showed that GMM susceptibility to noise remained stable within the tunable range of both RTL and USRP sensors.

*4) **Bookkeeping**:* At each iteration, we apply stopping criteria and update the detection state (steps 6-7). The bookkeeping process proceeds as follows:

(1) *Report time-frequency occupancy*: $\mathbf{T}_i = \mathbf{g}\mathbf{d}_s^\top$.

(2) *Stopping Criterion* (step 6): Classify the detection as a transmitter if its average power $\overline{\mathbf{X}(\mathbf{T_i})}$ exceeds the q-quantile of a precomputed noise distribution (estimated once by sampling $\mathbf{X}$); otherwise, discard as noise and terminate. The threshold q balances detection sensitivity versus false positives. For low-SNR harmonic detection, we set $q = 0.3$ (Section V-E), which tolerates higher false positives since the spatial position of detected activity across bands enables post-hoc discrimination of true harmonics from false detections.

(3) *Updating the Detection Mask* (step 7): If the stopping condition is not met, the detection mask and result set are updated per (Eq. (15)) and the iterative transmitter discovery continues.

$$\mathbf{\Omega} = \max(\mathbf{\Omega} - \mathbf{T}_i, 0), \quad \mathbf{T} = \mathbf{T} \cup \mathbf{T}_i \tag{15}$$

D. Reconciliation and classification

The goal of *harmonic reconciliation* is to couple fundamental and harmonic activity based on their similarity. The *harmonic classification*, in turn, seeks to blindly determine whether an observed activity is fundamental or harmonic, and determine the harmonic order. We detail these in turn.

1) Similarity-based reconciliation.: Given an observed transmission $\mathbf{T}^k$ in the k-th tensor slice, we compute the pairwise similarity between it and each transmitter $\mathbf{T}_i^n$ detected in the other $(k-1)$ tensor slices. Our similarity measure derives from the Jaccard Index as follows:

$$s(\mathbf{T}_i^n, \mathbf{T}^k) = \frac{|\mathbf{T}_i^n \cap \mathbf{T}^k|}{|\mathbf{T}_i^n \cup \mathbf{T}^k|} \tag{16}$$

Where $n \in [1, k-1]$, and $\mathbf{T_i^n}$ and $\mathbf{T^k}$ are the set of pixels detected as occupied. Using a pre-set similarity threshold ξ, we flag tensor slices in which highly-similar activity was observed. This results in a binary co-occurrence vector $\mathbf{s} \in \mathbb{R}^{k-1}$ where 1s denote all tensor slices carrying the same activity.

2) Observation classification: As detailed in Sec. III, and illustrated in Fig. 2, different observed cases (fundamental vs. harmonics) will result in a distinct co-occurrence vector. We pre-compute the expected co-occurrence patterns for all target cases, and use them against the computed co-occurrence vectors $\mathbf{s}$ to classify an observed activity as fundamental or harmonic, and discern the harmonic order.

E. Computational Complexity

The algorithmic complexity of `M-SHarC` is dominated by steps 4 and 5 in Alg.1. At each reverse step per signal component R, the algorithm performs: 1. **Forward pass through the U-Net** which costs: $\mathcal{O}\left(D_s \times C^2 \times t \times f\right)$ where: D_s is the number of U-Net layers, and C is the number of channels per layer. 2. **Forward pass through the FCN** which costs: $\mathcal{O}\left(L_c \times W^2 + W \times k\right)$ where: L_c is the number of FCN layers, W is the hidden layer width, $W \times k$ is the cost of the final layer mapping to band dimension k. 3. **Outer product** to combine the U-Net and FCN costs $\mathcal{O}(t \times f \times k)$. The total cost per signal component is: $\mathcal{O}\left(D_s C^2 tf + L_c W^2 + Wk + tfk\right)$, and the total complexity for all R signal components, over τ_0 reverse steps is: $\mathcal{O}\left(\tau_0 \times R \times \left(D_s C^2 tf + L_c W^2 + Wk + tfk\right)\right)$. For a small k we can simplify to: $\mathcal{O}\left(\tau_0 \times R \times \left(D_s C^2 tf\right)\right)$. We evaluate `M-SHarC`'s runtime in Sec. V-D.

V. Evaluation

A. Experimental setup and data

Data. We evaluate `M-SHarC` on synthetic and OTA data. The dataset is represented as a three-way tensor $\mathcal{X} \in \mathbb{R}^{t \times f \times k}$, where each slice corresponds to RF data $\mathbf{X} \in \mathbb{R}^{t \times f}$. The first slice represents data in the fundamental frequency band, while the remaining slices capture harmonic bands, as described in Eq. (1). For synthetic data, the tensor slices are generated as 2D matrices of PSD values drawn from $b+1$ normal distributions $\mathcal{N}_i(\mu_i, \sigma_i^2)$, where $i \in [1, b]$ represents the number of transmitters, and μ_i and σ_i^2 denote the mean and variance of the i-th signal. The specific transmitter distributions are detailed in their respective experiments. Noise is generated from the $\mathcal{N}_{b+1}$-th distribution, with a mean of -109 dBm and a standard deviation of 5, informed by empirical measurements of the noise floor of a USRP B210 software-defined radio.

For our controlled OTA datasets, we built a testbed of one transmitter (USRP B210 radios with PCB log-periodic directional antenna and a laptop host) and two sensors (USRP B210 radio, PCB log-periodic directional antenna and laptop host). The collected data consists of IQ samples, which are converted to PSD using a GNURadio script. From the PSD data, we generate a signal bank with transmitter and noise distributions, which is sampled to create transmitter signals and noise for specific experiments. Details on the signal and noise characteristics are provided within each experiment.

For each i-th harmonic/transmitter in tensor slice n we store ***groundtruth*** $\mathbf{G}_i^n$ as a binary matrix with 1s indicating time-frequency bins in which the target transmitter/harmonic occurs. Since our method is unsupervised, the groundtruth is only used in our evaluation to compute detection accuracy.

Baselines. We compare `M-SHarC` with SCAN [14], AirVIEW[13], and TxMiner [12]. Since AirView is designed for single-transmitter detection, we exclude it from evaluations involving multiple transmitters.

Metrics. To evaluate our transmitter/harmonic characterization, we use an accuracy measure (J) inspired by the Jaccard Index. Specifically, J measures the similarity between detected harmonics $\mathbf{T}^n$ and their respective ground truth $\mathbf{G}^n$ as:

$$J = 100 \times \frac{|\mathbf{T}^n \cap \mathbf{G}^n|}{|\mathbf{T}^n \cup \mathbf{G}^n|} \tag{17}$$

Here $n \in [1, k]$ represents the tensor slices. This accuracy measure varies between 0% and 100%, with 0% indicating no overlap between the detected transmitter and its groundtruth, and 100% indicating a full overlap between the two.

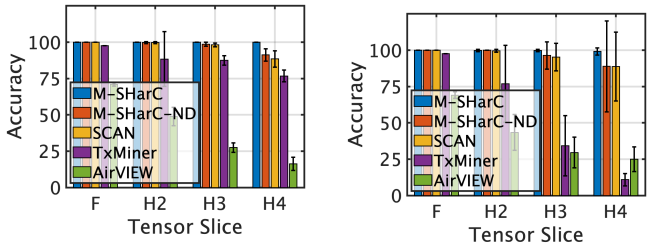

Figure 4: Characterization accuracy with incumbent-free harmonic slices in low-SNR scenarios using synthetic data (left) and OTA data (right).

Implementation. M-SHarC's denoising step (Sec. IV-B1) is implemented in Python and ran on a NVIDIA A40 GPU that has CUDA version 12.8. The characterization step (Sec. IV-C) is implemented in MATLAB and ran on a MacBook Pro that has an Apple M2 chip, 24 GB RAM, and macOS 15.0.1.

B. Accuracy in harmonic characterization

Detection of non-interfering harmonics. We demonstrate M-SHarC's ability to detect faint harmonic emissions in frequency bands without actively transmitting incumbents. This setting is particularly relevant to passive/scientific observers, whose applications are negatively affected by harmonic interference. We generate four-slice tensors in which the first slice corresponds to an observation at frequency f Hz, and the subsequent slices capture harmonic components at $2f$, $3f$, and $4f$. Across successive slices, the average harmonic power progressively degrades toward the noise floor. We evaluate performance in low-SNR regimes, where the fundamental averages 16 dB above the noise floor and the harmonics in slices two, three, and four average 6 dB, 4 dB, and 3 dB above the noise floor, respectively.

Fig. 4 reports the mean and standard deviation of the characterization accuracy over 10 runs (Eq. (17)) for each tensor slice using synthetic data (left) and over-the-air (OTA) measurements (right). We compare M-SHarC against three baseline methods from the literature, as well as a variant without diffusion-based denoising (M-SHarC-ND).

M-SHarC consistently outperforms all baselines and maintains high characterization accuracy even for the faintest harmonic components, including H3 at 4 dB SNR and H4 at 3 dB SNR. In contrast, prior methods degrade substantially for higher-order harmonics, particularly in OTA scenarios. Diffusion-based denoising further enhances performance for high-order harmonics, yielding near-ideal characterization and up to a 15% improvement over the undenoised variant. Overall, while existing methods can perform well when harmonics are isolated and moderately above the noise floor, M-SHarC provides robust and reliable harmonic characterization in low-SNR and real-world measurement settings.

Detection of interfering harmonics. We next consider scenarios in which harmonic emissions co-occur with high-power incumbent activity. M-SHarC currently assumes no frequency overlap between harmonics and incumbent activity; handling full time-frequency overlap is left for future work.

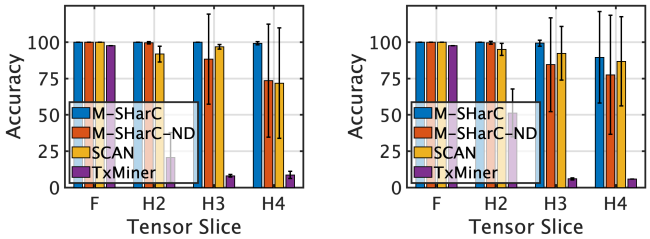

Figure 5: Characterization accuracy with incumbents in harmonic slices with low SNR using synthetic (left) and OTA data (right).

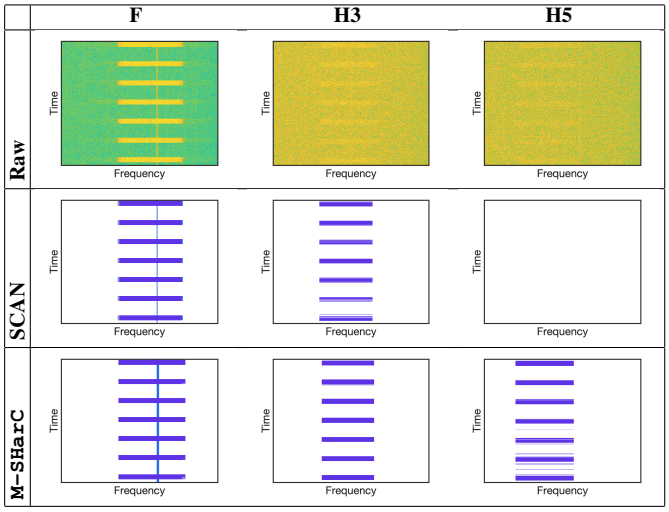

Table I: Real-world harmonic characterization in a lab testbed. The top row presents the raw spectrograms, while the middle and bottom rows show SCAN and M-SHarC characterizations, respectively. Fundamental was captured at an average SNR of 22dB; H3 at 3.1dB and H5 at 2dB.

Fig. 5 reports the mean characterization accuracy with standard deviation error bars over 10 runs for synthetic data (left) and over-the-air (OTA) measurements (right). Since AirVIEW does not support multi-transmitter scenarios, we exclude it from the comparison and evaluate against TxMiner, SCAN, and a variant of M-SHarC without diffusion-based denoising (M-SHarC-ND). The transmitter power levels are 16 dB, 6 dB, 4 dB, and 3 dB above the noise floor for the fundamental and successive harmonic orders. M-SHarC outperforms all baseline methods across all cases, although its first performance degradation appears in OTA measurements for the fourth-order harmonic (H4). This degradation is attributable to a sample in which the harmonic power falls below 2 dB above the noise floor, resulting in a missed characterization. Overall, these results highlight M-SHarC's robustness in faint harmonic detection even in the presence of active incumbent transmissions.

Qualitative evaluation in a lab testbed. We conducted a real-world experiment using multiple USRP B210 devices equipped with log-periodic antennas to evaluate harmonic detection in a real-world setting. One USRP acted as the transmitter, periodically sending 1 kilobyte bursts at 460 MHz with a 400 ms idle period between transmissions. Two additional USRPs, placed approximately 20 feet away, were configured as receivers. One was tuned to the transmitter's fundamental frequency (460 MHz), while the other was configured to

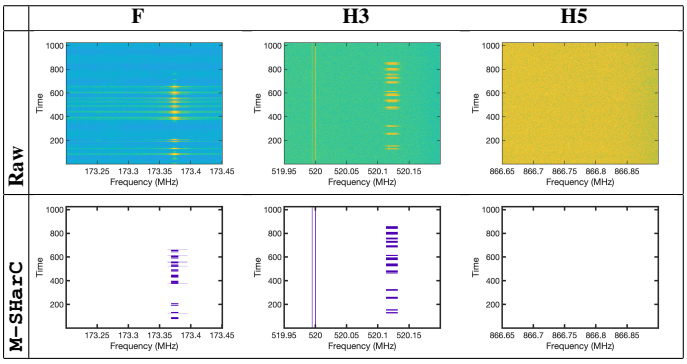

Table II: Real-world harmonic characterization of a public safety transmitter. The top row shows the raw spectrograms, and the bottom row shows the corresponding M-SHarC characterization results.

consecutively capture its 3rd and 5th harmonics at 1380 MHz and 2300 MHz, respectively. The SNR for the fundamental, 3rd, and 5th harmonics were 22.36 dB, 3.09 dB, and 2.2 dB respectively. Due to only having three USRPs, harmonic slices were captured sequentially rather than concurrently, although ideally all bands would be observed simultaneously. We focus on odd harmonics (3rd and 5th) since even harmonics were not detectable above the noise floor for our setup, likely due to hardware symmetry that provides even harmonic suppression. As ground truth is not available in this setup, we present a qualitative visual evaluation. Table I presents the spectrograms observed at the fundamental and harmonic frequencies, along with their corresponding characterizations produced by our top-performing baseline SCAN and M-SHarC. M-SHarC successfully detects the transmitter at the fundamental frequency and both harmonics. In contrast, SCAN detects the transmitter and the 3rd harmonic but fails to identify the 5th harmonic.

C. Real-world applicability.

We collected real-world spectrum measurements within the NRQZ[47], approximately 16 km from the Green Bank Observatory[48]. Our measurements targeted a public safety transmitter located about 75 meters from the measurement location. We used a USRP B210 with an EM-6950 Log Periodic antenna and a laptop to collect signals at the transmitter's fundamental, 3rd and 5th harmonic bands at 173.37 MHz, 520.11 MHz, and 866.85 MHz, respectively. Due to antenna constraints, measurements at the different frequencies were conducted sequentially rather than concurrently. As a result, the captures presented next are not time-aligned.

Table II presents the spectrograms of the raw spectrum traces (row 1) along with the corresponding transmitter characterization produced by M-SHarC (row 2). M-SHarC successfully detects the transmitter at its fundamental frequency and at the associated 3rd harmonic, and correctly reports no detection in the 5th harmonic band, where no harmonic emission from the transmitter is present.

D. Denoising considerations

So far, we explored the performance benefits of diffusion-based denoising. We now set off to explore two issues: computational cost and denoising hallucinations.

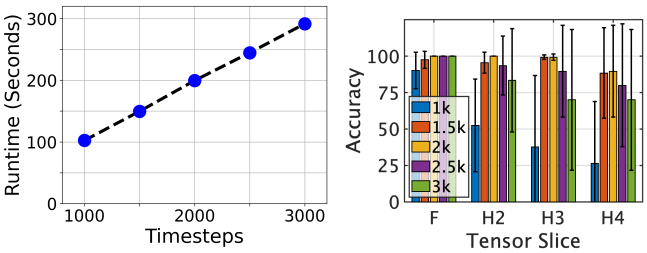

Figure 6: Runtime and accuracy across denoising steps. The runtime increases linearly. The optimal performance for our datasets was at $2,000$ steps.

Slice	Slice2 is Noise	Slice 3 is Noise	Slice 4 is Noise
1	100	100	100
2	5.55	100	100
3	100	1.96	99.89
4	99.57	99.04	2.37

Table III: Characterization accuracy for isolated harmonic low SNR scenario when one slice is replaced with pure noise. No "hallucinations" were observed.

Effects of denoising iterations on computational cost. The number of timesteps τ in the denoising process affects M-SHarC's performance in two ways. First, the accuracy deteriorates with too few or too many steps. Runtime too depends on the time spent denoising. Therefore, it is advisable to use the lowest number of timesteps possible without sacrificing performance. Using our most challenging scenario – OTA low SNR with incumbents, we explored accuracy and runtime while increasing the denoising steps (Fig 6). The runtime increases linearly with the number of iterations (left). Furthermore, the optimal performance for our datasets occurs at 2000 steps (right), while at higher numbers of steps, the denoising process over-smooths the data resulting in worse results. Based on these two results, we use 2000 denoising timesteps for all results presented so far.

Denoising hallucinations. A key concern with our problem setting is whether the diffusion-based denoising process might produce signal artifacts that resemble transmitter activity but were not present in the original spectrum scans (we refer to those as hallucinations). To test our methodology for resilience against this potential problem, we ran an experiment using our OTA dataset but we replaced some previously-occupied slices with pure noise. We tested M-SHarC with this new dataset and present the results in Table III. We see that slices that were comprised of noise have characterization accuracies close to zero meaning that M-SHarC does not classify harmonics where none exists (does not create signal "hallucinations").

E. Activity type classification

We now employ M-SHarC to reconcile a potential harmonic signal with its source, and classify its order following the general problem setting of multi-spectral transmitter analytics presented in Sec. III and Fig. 2. Specifically, given a signal observed at some frequency f, we attempt to classify it as fundamental (*Case 1* – C1), 2nd order harmonic (*Case 2* – C2), 3rd order harmonic (*Case 3* – C3), or 4th order harmonic (*Case 4* – C4). This problem setting results in six unique spectral slices (at frequencies $1/4f$, $1/3f$, $1/2f$, $2/3f$, $3/4f$

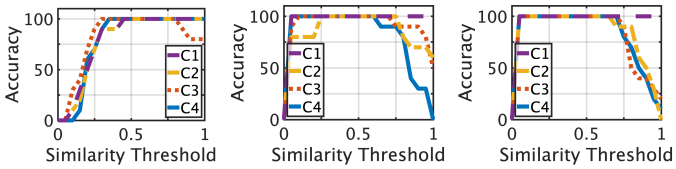

Figure 7: Accuracy in blindly classifying an observed activity as either fundamental (C1), or second (C2), third (C3), and fourth (C4) order harmonic with increasing similarity threshold ξ for incumbent-free (left), single incumbent per slice (middle), and two incumbents per slice (right).

and f), which need to be concurrently observed to support the classification process (Fig. 2). As detailed in Sec. III, each of the four cases (C1–C4) will result in a distinct spectrum activity across these six slices, whereby some slices will feature transmitter/harmonic activity and others will not. Per Sec. IV-D1, we store these cross-tensor activity patterns in a co-occurrence vector $\mathbf{s}$, which can be used to classify which of the four cases is observed at frequency f.

For this experiment, we created a separate dataset with 6-slice tensors (we refer to each tensor as one observation) using our low SNR OTA data. For these datasets, the average SNR of incumbents was 26dB. The power level of the harmonic transmitter matches that of the OTA incumbent low SNR scenario as follows. If the transmitter is the fundamental signal, its power level averages 17 dB above the noise floor. If it is a second harmonic it averages 7dB above the noise floor, third harmonic averages 5dB above the noise floor, and fourth harmonic averages 4dB above the noise floor. We explore three scenarios: (i) with no incumbents, (ii) with one incumbent per tensor slice and (ii) with two incumbents per slice. For each of these settings, we generate 40 observations, 10 for each of the cases C1-C4. We then characterize this dataset using `M-SHarC`, with a further relaxation of the stopping criteria, which for this experiment was set to $q = 0.5$. This ensured that harmonics are detected despite the increased complexity of the characterization task. We then produce the corresponding $\mathbf{s}$ co-occurrence vectors across a range of similarity thresholds ξ. Finally, we use the co-occurrence vectors to classify which of the four cases was observed in frequency f, following the expected co-occurrence patterns from Fig. 2. Fig. 7 presents our results across the three scenarios. On the x-axis of each of the figures, we vary the similarity threshold ξ, which is used to produce the $\mathbf{s}$ co-occurrence vectors. On the y-axis, we present classification accuracy, as the ratio between correctly-classified observations vs. the total number of observations per case. The four curves in each figure correspond to the four target cases C1–C4. We see that above a similarity threshold of 0.7, the classification accuracy begins to decline, especially when the observation captures farther-away faint harmonics (i.e. second and third) in the presence of more than one incumbents. This can be explained with `M-SHarC`'s characterization performance declining with farther-away harmonics and in the presence of increasing incumbents, which results in only a subset of the harmonic being detected. This is where lowering the similarity measure ξ (i.e. relaxing the required similarity between observed and other related activity) can be helpful. As can be seen in these results, if we require no more than 70% resemblance between an observation and it's related out-of-band activities, we can achieve 100% classification accuracy regardless of the number of incumbents present. The selection of the similarity threshold will vary, depending on the application developer, with some applications being more willing to relax the similarity requirement than others.

VI. Discussion and Conclusion

The densification of wireless devices, compounded by their increasing complexity, creates multi-spectral coexistence problems, increased RF noise pollution and interference from out-of-band emissions. For next-generation spectrum coexistence, noise/interference issues should be considered across multiple spectra. This paper conceptualized multi-spectral transmitter analytics and designed `M-SHarC` to detect and reconcile harmonics over multiple spectra. We focused on harmonic reconciliation, however, other out-of-band effects (i.e. sideband emissions and receiver spurs) should also be considered. While our efforts focused on harmonics co-occurring with incumbents, we have not yet explored partial or full time-frequency overlap of incumbents and harmonics. Lastly, depending on the case, the number of concurrently-scanned bands may grow substantially. Some supervision in the detection process can help minimize the sensing cost.

This work establishes a foundation for multi-spectral radio analytics using `M-SHarC`. `M-SHarC` employs a self-supervised diffusion model for spectrum scan denoising, which alleviates the requirements for extensive model training, while also ensuring denoising robustness in unseen scenarios. Furthermore, `M-SHarC` uses multi-dictionary sparse coding for high-sensitivity unsupervised detection of faint harmonics, and is thus applicable to arbitrary transmitter technologies. Evaluation through simulation and over-the-air USRP traces demonstrates that `M-SHarC` consistently outperforms literature counterparts in extremely low-SNR regimes (harmonics as low as 3 dB above the noise floor) while classifying activity type in arbitrary observations. We also demonstrated `M-SHarC`'s applicability to real-world scenarios following harmonic a measurement campaign in the National Radio Quiet Zone. This work can impact next-generation spectrum coexistence and enforcement by enabling profiling and reconciliation of harmful interference from out-of-band emissions, thereby improving commercial, scientific and defense applications of the radio spectrum.

References

[1] M. Zheleva *et al.*, "Radio dynamic zones: Motivations, challenges, and opportunities to catalyze spectrum coexistence," *IEEE Communications Magazine*, 2023.

[2] A. Acakpovi *et al.*, "Impact analysis of induced FM radio interferences on aeronautical radio navigation systems: case study of Kotoka international airport, Accra-Ghana," in *IEEE ICCMA 2019*, Cape Coast, Ghana, 2019.

[3] N. A. of Broadcasters, "FM 8th Harmonic Interference to Wireless Facility Not Radiated by the FM Station: A Case Study," https://nabpilot.org/fm-8th-harmonic-interference-to-wireless-facility-not-radiated-by-the-fm-station-a-case-study/.

[4] A. Ghasemi and E. S. Sousa, "Interference aggregation in spectrum-sensing cognitive wireless networks," *IEEE Journal of Selected Topics in Signal Processing*, vol. 2, no. 1, pp. 41–56, 2008.

[5] S. Tschimben *et al.*, "Testbed for radio astronomy interference characterization and spectrum sharing research," in *IEEE Aerospace Conference*, Big Sky, MT, USA, 2023, pp. 1–16.

[6] M. Spencer and F. Ulaby, "Spectrum issues faced by active remote sensing: Radio frequency interference and operational restrictions technical committees," *IEEE Geoscience and Remote Sensing Magazine*, 2016.

[7] S. Misra and P. de Matthaeis, "Passive remote sensing and radio frequency interference (RFI): An overview of spectrum allocations and RFI management algorithms [technical committees]," *IEEE Geoscience and Remote Sensing Magazine*, vol. 2, no. 2, pp. 68–73, 2014.

[8] A. Chaman *et al.*, "Ghostbuster: Detecting the presence of hidden eavesdroppers," in *ACM MobiCom 2018*, New York, NY, 2018, pp. 337–351.

[9] M. Mesarcik *et al.*, "Learning to detect radio frequency interference in radio astronomy without seeing it," *Monthly Notices of the Royal Astronomical Society*, vol. 516, no. 4, pp. 5367–5378, 2022.

[10] A. Madanayake *et al.*, "AI/ML interference cancellation used in STAR wireless for radio astronomy RFI control," in *2024 IEEE International Conference on Microwaves, Communications, Antennas, Biomedical Engineering and Electronic Systems (COMCAS)*, 2024, pp. 1–6.

[11] F. Di Vruno *et al.*, "Unintended electromagnetic radiation from starlink satellites detected with lofar between 110 and 188 mhz," *Astronomy & Astrophysics*, vol. 676, p. A75, 2023.

[12] M. Zheleva *et al.*, "TxMiner: Identifying transmitters in real-world spectrum measurements," in *2015 IEEE International Symposium on Dynamic Spectrum Access Networks (DySPAN)*, Stockholm, Sweden, 2015, pp. 94–105.

[13] M. Zheleva *et al.*, "AirVIEW: Unsupervised transmitter detection for next generation spectrum sensing," in *IEEE INFOCOM 2018-IEEE Conference on Computer Communications*, Honolulu, HI, USA, 2018, pp. 1673–1681.

[14] B. Okoro *et al.*, "Sparse Recovery Transmitter Detection," in *IEEE INFOCOM 2025-IEEE Conference on Computer Communications*, London, United Kingdom, 2025, pp. 1–10.

[15] K. Doke *et al.*, "RadVIEW: Robust radar detection and characterization in high-noise regimes," in *2024 IEEE International Symposium on Dynamic Spectrum Access Networks (DySPAN)*, Washington, DC, USA, 2024, pp. 1–8.

[16] N. Soltani *et al.*, "Finding waldo in the CBRS band: Signal detection and localization in the 3.5 GHz spectrum," in *IEEE GLOBECOM 2022*, Rio de Janeiro, Brazil, 2022, pp. 4570–4575.

[17] S. Sarkar *et al.*, "DeepRadar: A deep-learning-based environmental sensing capability sensor design for CBRS," in *ACM MobiCom 2021*, New York, NY, USA, 2021, pp. 56–68.

[18] D. Uvaydov *et al.*, "Stitching the Spectrum: Semantic Spectrum Segmentation with Wideband Signal Stitching," in *IEEE INFOCOM 2024*, Vancouver, BC, Canada, 2024.

[19] P. Panagiotou *et al.*, "Likelihood ratio tests for modulation classification," in *MILCOM 2000*, vol. 2, Los Angeles, CA, USA, 2000, pp. 670–674.

[20] W. Xiong *et al.*, "Robust and efficient modulation recognition based on local sequential IQ features," in *IEEE INFOCOM 2019*, Paris, France, 2019, pp. 1612–1620.

[21] A. Nika *et al.*, "Empirical validation of commodity spectrum monitoring," in *ACM SenSys 2016*, New York, NY, USA, 2016, pp. 96–108.

[22] A. Chakraborty *et al.*, "SpecSense: Crowdsensing for efficient querying of spectrum occupancy," in *IEEE INFOCOM 2017*, Atlanta, GA, USA, 2017, pp. 1–9.

[23] S. Rajendran *et al.*, "Unsupervised wireless spectrum anomaly detection with interpretable features," *IEEE Transactions on Cognitive Communications and Networking*, vol. 5, no. 3, pp. 637–647, 2019.

[24] Z. Li *et al.*, "Scaling deep learning models for spectrum anomaly detection," in *ACM MobiHoc 2019*, New York, NY, USA, 2019, pp. 291–300.

[25] K. Merchant *et al.*, "Deep learning for RF device fingerprinting in cognitive communication networks," *IEEE Journal of Selected Topics in Signal Processing*, vol. 12, no. 1, pp. 160–167, 2018.

[26] Y. Miao *et al.*, "DDS2M: Self-supervised denoising diffusion spatio-spectral model for hyperspectral image restoration," in *ICCV 2023*, Paris, France, 2023, pp. 12 086–12 096.

[27] "USRP," https://www.ettus.com/.

[28] E. Perenda *et al.*, "Learning the unknown: Improving modulation classification performance in unseen scenarios," in *IEEE INFOCOM 2021*, Vancouver, BC, Canada, 2021, pp. 1–10.

[29] E. Perenda *et al.*, "Contrastive learning with self-reconstruction for channel-resilient modulation classification," in *IEEE INFOCOM 2023*. New York, NY: IEEE, 2023, pp. 1–10.

[30] J. Kim *et al.*, "A CMOS direct conversion transmitter with integrated in-band harmonic suppression for IEEE 802.22 cognitive radio applications," in *2008 IEEE Custom Integrated Circuits Conference*, San Jose, CA, 2008, pp. 603–606.

[31] S. Roshani *et al.*, "Design of a modified compact coupler with unwanted harmonics suppression for l-band applications," *Electronics*, vol. 11, no. 11, p. 1747, 2022.

[32] T. Guo *et al.*, "A review of wavelet analysis and its applications: Challenges and opportunities," *IEEE Access*, vol. 10, pp. 58 869–58 903, 2022.

[33] G. R. Sahoo *et al.*, "Optimal wavelet selection for signal denoising," *IEEE Access*, vol. 12, pp. 45 369–45 380, 2024.

[34] K. Ferroudji *et al.*, "Selection of a suitable mother wavelet for microemboli classification using SVM and RF signals," in *2012 IEEE ICM*, Algiers, Algeria, 2012, pp. 1–4.

[35] Y. Wang *et al.*, "RF fingerprint recognition based on adaptive wavelet threshold denoising," in *IEEE ICCC 2024*, Hangzhou, China, 2024, pp. 337–342.

[36] W. Nie *et al.*, "UAV detection and identification based on WiFi signal and RF fingerprint," *IEEE Sensors Journal*, vol. 21, no. 12, pp. 13 540–13 550, 2021.

[37] C. Bertoncini *et al.*, "Wavelet fingerprinting of radio-frequency identification (RFID) tags," *IEEE Transactions on Industrial Electronics*, vol. 59, no. 12, pp. 4843–4850, 2011.

[38] E. Almazrouei *et al.*, "Using autoencoders for radio signal denoising," in *ACM Q2SWinet 2019*, Miami Beach, FL, USA, 2019, pp. 11–17.

[39] S. Subray *et al.*, "Towards enhancing spectrum sensing: Signal classification using autoencoders," *IEEE Access*, vol. 9, pp. 82 288–82 299, 2021.

[40] J. Woo *et al.*, "Noise-adaptive auto-encoder for modulation recognition of RF signal," in *IEEE/MTT-S International Microwave Symposium-IMS 2024*, Washington, DC, USA, 2024, pp. 820–823.

[41] J. Yu *et al.*, "Radio frequency fingerprint identification based on denoising autoencoders," in *IEEE WiMob 2019*, Barcelona, Spain, 2019, pp. 1–6.

[42] J. Ho *et al.*, "Denoising diffusion probabilistic models," in *ACM NIPS 2020*, Vancouver, BC, Canada, 2020, pp. 6840–6851.

[43] B. Kawar *et al.*, "Denoising diffusion restoration models," in *ACM NIPS 2022*, New Orleans, LA, USA, 2022, pp. 23 593–23 606.

[44] G. Chi *et al.*, "RF-diffusion: Radio signal generation via time-frequency diffusion," in *ACM MobiCom 2024*, Washington, DC, USA, 2024, pp. 77–92.

[45] X. Wang *et al.*, "Erasing noise in signal detection with diffusion model: From theory to application," *arXiv preprint arXiv:2501.07030*, 2025.

[46] K. Doke *et al.*, "VIA: Establishing the link between spectrum sensor capabilities and data analytics performance," in *IEEE INFOCOM 2024*, Vancouver, BC, Canada, 2024, pp. 2229–2238.

[47] NRAO, "National radio quiet zone," https://info.nrao.edu/do/spectrum-management/national-radio-quiet-zone-nrqz-1.

[48] "Green bank observatory," https://greenbankobservatory.org/.